Detailed modelling of alpha transport due to ELM control fields in ITER: implications for PFCs and diagnostic design

F. Camilo de Souza[1], K. G. McClements[1], A. Prokopyszyn[1], A. Snicker[2], A. Reyner-Viñolas[3], J. Gonzalez-Martin[4], L. Sanchis-Sanchez[3], R. Marques[4]

[1]United Kingdom Atomic Energy Authority, UKAEA, Culham Campus Abingdon OX14 3DB UK
[2]Dept. of Applied Physics, Aalto University, FI-00076, Aalto, Finland
[3]Dept. of Atomic, Molecular and Nuclear Physics, University of Seville, Seville, Spain
[4]Dept. of Mechanical and Manufacturing Engineering, University of Seville, Seville, Spain

E-mail: fabio.camilo.de.souza@ukaea.uk

February 2026

Abstract. This paper presents simulations of alpha-particle transport in ITER driven by static 3D magnetic field perturbations in the high-performance 15 MA $Q = 10$ baseline scenario, specifically resonant magnetic perturbations (RMPs) arising from edge-localized mode (ELM) control coils, combined with toroidal field ripple (TFR) and effects from ferromagnetic materials. We employ the Lorentz-Orbit Code for Use in Stellarators and Tokamaks (LOCUST), which tracks fast-ion orbits under the Lorentz force and Monte Carlo collisions with the bulk plasma, taking into account the detailed geometry of ITER plasma-facing components (PFCs). LOCUST uses GPU cards to enable the high-resolution modelling required to accurately resolve power fluxes across surfaces with complex morphologies, including unprotected cooling pipes beneath the dome divertor, and the generation of reliable synthetic diagnostics for the ITER Fast Ion Loss Detector (FILD) to support its design. The simulations include a range of ELM control coil current profiles with toroidal mode number N=3. The results indicate that the total alpha-particle energy loss has a negligible impact on plasma performance, remaining below 1% of the alpha energy produced in D–T reactions. Furthermore, the power flux density on the divertor structures and the first wall remains well below design limits and is comparable to thermal and radiative loads. The simulated alpha flux on the FILD scintillator plate is well above the noise threshold and can be significantly higher than conservative estimates.

1. Introduction

In the 15MA $Q = 10$ baseline scenario, ITER is designed to generate 500MW of fusion power, of which 100 MW is released in the form of fusion alpha-particles [1]. These particles will constitute the largest source of heating in the device, and the plasma will thus be in a nuclear burning state. The pedestal characteristics of the baseline scenario trigger type-I Edge-Localized Modes (ELMs) [2, 3], which can degrade plasma performance and expose plasma-facing components (PFCs) to damage [4], thereby threatening operational efficiency and longevity of the device. To address this issue, ITER will be equipped with three sets of ELM control coils (ELMcc) [5, 6, 7, 8, 9], which generate resonant magnetic perturbations (RMPs) intended to mitigate ELMs by breaking the plasma's axial symmetry.

Static 3D magnetic perturbations, such as RMPs, violate the conservation of canonical momentum and consequently lead to the transport of energetic particles [10, 11, 12, 13, 14]. Naturally, this transport is most significant in regions where RMPs have the highest amplitude, namely at the plasma edge. The majority of alpha-particles are generated by D-T reactions near the plasma core and are therefore unaffected by these perturbations. However, due to the pedestal configuration, which exhibits high temperature and density even far from the core, a non-negligible fraction of alpha-particles is produced close to the plasma edge. The transport of this minority of the total alpha-particle population can lead to concentrated power fluxes on PFCs. The distribution of power flux on PFCs is strongly influenced by both the configuration of the ELMcc currents and the plasma response to these currents.

Concentrated power fluxes can potentially lead to erosion or blistering of PFCs, resulting in material degradation [15]. Moreover, since the majority of PFCs in ITER are made of tungsten, sputtering due to alpha-particle impacts presents an additional concern. This sputtering can increase the impurity content and effective charge of the plasma, thereby degrading overall fusion performance due to fuel dilution and radiative losses. The sputtering yield depends on the energy [16] of the impacting particles and their angle of incidence [17], which is strongly influenced by the complex surface morphology of the PFCs.

Monitoring of these alpha-particle losses will be performed in ITER using a Fast Ion Loss Detector (FILD) [18, 19, 20]. The FILD provides energy and pitch angle spectroscopy of the lost alpha-particles over time, enabling different sources of energetic particle transport in both static and time-dependent perturbations to be distinguished [21]. Alpha-particles enter the FILD through a small pinhole, are collimated, and then strike a scintillator plate, which emits photons that are captured by a camera. The design of the pinhole and collimator directly affects the measurement: more constricted apertures improve energy/pitch resolution but may reduce the alpha-particle flux on the scintillator to levels that are difficult to distinguish from noise, while a less constricted design degrades the resolution of the strike map. The ITER FILD will be positioned at the outer mid-plane and detect losses that are spatially localized in this region.

Simulations of the alpha-particle flux in the presence of static 3D fields are usually performed by simply following the orbits of energetic particles. The collisional slowing-down of alpha-particles in the ITER baseline scenario takes on the order of 1 s to complete and the orbits must be tracked within the complex geometry of the PFCs. Therefore, simulating a realistic ITER scenario is especially challenging and computationally expensive. The Lorentz-Orbit Code for use in Stellarators and Tokamaks (LOCUST) [22, 23] offers a potential solution by enabling high-fidelity energetic ion orbit tracking, massively parallelized on GPU systems. This capability facilitates the simulation of alpha-particle transport driven by ELM mitigation fields, making it possible to quantify damage to PFCs and supporting FILD design through the production of reliable synthetic diagnostics.

This work investigates the impact of the ELM mitigation strategy on fusion alpha-particle heating efficiency and localized power fluxes on PFCs. Using LOCUST, we calculate the alpha-particle loss distributions under applied RMPs using detailed models of ITER PFCs. We also include the effects of toroidal field ripple (TFR), which are mitigated by ferromagnetic inserts and further modified by the presence of tritium breeding test blanket modules. Although the TFR impact on overall alpha-particle transport is negligible, the local redistribution near the midplane, where these perturbations are strongest, can significantly influence the alpha-particle flux detected by the FILD.

To compute the effects of 3D field perturbations on alpha-particle confinement, LOCUST follows the orbits of markers representing alpha-particles from their birth in the D–T reaction until thermalization or collision with any PFC. LOCUST employs the Boris leapfrog algorithm to integrate the Lorentz equations of motion, including Monte Carlo collisions with thermal plasma particles.

The present study complements a series of publications: [24, 25] using LOCUST to study neutral beam ion losses, and [19, 26, 27] employing ASCOT to model both neutral beam and alpha-particle losses. The main difference between the simulations performed in each code lies in their treatment of particle orbits: ASCOT uses the guiding-centre approximation, whereas LOCUST performs full-orbit integration. The full-orbit approach is more reliable when field perturbations occur on length scales comparable to the particle gyro-radius, such as the fields arising from the plasma response to RMPs. Furthermore, the GPU parallelization in LOCUST enables detailed modelling of all ITER PFCs, including divertor structures, and allows the use of a very large number of markers representing alpha-particles, producing high-resolution

heat flux maps.

In Section 2 we introduce in detail the 3D fields included in the simulations, their contribution to alpha-particle transport, and the resulting impact on plasma performance. In Section 3 we present the peak power fluxes densities on each PFC, while in Section 4 we discuss optimization of the FILD through the construction of synthetic diagnostics employing FILDSIM [28] code.

2. Static 3D fields and associated alpha-particle transport

Static 3D magnetic perturbations violate conservation of the toroidal canonical momentum of energetic particles, causing some orbits to become unconfined and leading to transport that deposits energy on the PFCs [10, 11, 12].

The ELM control fields and toroidal field ripple [26] are calculated by integrating the Biot–Savart law over the coil geometry. The plasma response is included to simulations, as detailed in section 2.2. The contribution of the ferromagnetic components [26] requires the use of the finite element method with non-linear magnetic material properties.

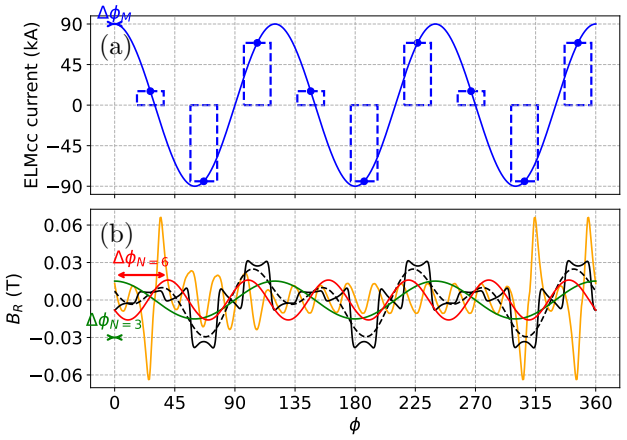

Figure 1: a) Illustration of the coil current profile of the middle set with $\Delta\phi_M = 0°$. The dashed lines show the current in each coil. b) The solid black curve shows the radial component of the ELM control field at the mid-plane on the LCFS. The solid green curve is the $N = 3$ component, the solid red curve is the $N = 6$ component, and the dashed black curve represents the sum of the $N = 3$ and $N = 6$ components. The yellow curve shows the fields arising from TFR and ferromagnetic materials.

2.1. Impact of the coil current profile phase on alpha-particle transport

As far as alpha-particle transport is concerned, the most significant magnetic perturbations are the RMPs generated by the ELMcc. ITER will be equipped with three sets of nine ELMcc coils; lower, mid, and upper [5]. The nine coils in each set are uniformly distributed in toroidal angle ϕ, with the first coil of each set positioned at $\phi = 30°, 26.7°$ and $30°$ for the lower, mid, and upper sets, respectively (where $\phi = 0°$ corresponds to the centre of vacuum vessel Sector #1: ϕ increases anti-clockwise as seen from above). Furthermore, each ELMcc set individual coil supports a maximum current of 90 kAt. The current profile of each ELMcc set is optimized for ELM mitigation. The current profile is defined as:

$$I_{coil} = I_0 \cos(N_0[\phi_{\text{coil}} - \Delta\phi_{\text{set}}]) \qquad (1)$$

where I_0 is the maximum current of the ELMcc set, N_0 is the toroidal number of the current profile, ϕ_{coil} is the mean toroidal angle of each coil and $\Delta\phi_{\text{set}}$ is the phase of the coil current profile applied to the entire ELMcc set.

Although the intended toroidal mode number of the perturbation is the one defined by the current profile, the finite number of ELMcc coils per set (9 coils per set) gives rise to several toroidal sidebands that also affects transport[13, 29]. The most relevant sideband has a toroidal number $N_s = 9 - N_0$, which in many cases can be as intense as the main component. Moreover, due to the relative phase of the current profile and its relation to the coil positions, the characteristic phase of the sidebands differs from that of the main toroidal mode, shifting in the opposite direction of the applied phase. This relationship is given by:

$$\Delta\phi_s = \phi_{\text{coil=1}} - \frac{N_0}{N_s}(\Delta\phi_{\text{set}} - \phi_{\text{coil=1}}) \qquad (2)$$

where $\Delta\phi_s$ is the relative phase of the sideband, $\phi_{\text{coil=1}}$ is the toroidal position of the first coil in the set, and N_s is the toroidal mode number of the sideband.

Figure 1 illustrates the coil current profile with $N_0 = 3$ for the middle set and $\Delta\phi_M = 0°$, along with the radial magnetic field perturbation generated by the set, at the mid-plane and the TFR on the last closed flux surface (LCFS). The focus here is on the main toroidal mode number and the most relevant sideband generated by the coil set [13, 29]. Figure 2 shows the field strength of the sidebands penetrating the plasma toward the core.

According to figure 2, the main toroidal mode number and the most significant sideband ($N = 3$ and $N = 6$, respectively) are present throughout the plasma with comparable amplitudes. Other sidebands decay rapidly with increasing distance from the coils.

To calculate the overall alpha power lost, LOCUST tracks the orbits of 130 thousand markers representing alpha particles, from their production in the D–T reaction until they collide with the PFCs or thermalize. The impact of the most significant sidebands on alpha-particle transport is illustrated in figure 3.

When only the $N = 3$ mode is considered, alpha-particle energy losses clearly peak when the phase difference between the coil sets is maximized, at $\Delta\phi_{U,L} = 60°$, reaching approximately 0.7% of the alpha energy produced. When the $N = 6$ sideband is included, the maximum energy loss increases to

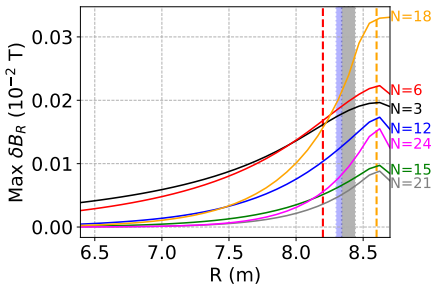

Figure 2: Illustration of the penetration of the magnetic field from each sideband, listed on the right side of the figure. The dashed yellow line indicates the position of the RMP coil set, the gray area denotes the first wall, the blue area shows the operational range of the FILD, and the dashed red line marks the LCFS. Magnitude at the vertical position of the FILD, $Z = 0.05\,\mathrm{m}$. The N=18 component arise from the TFR.

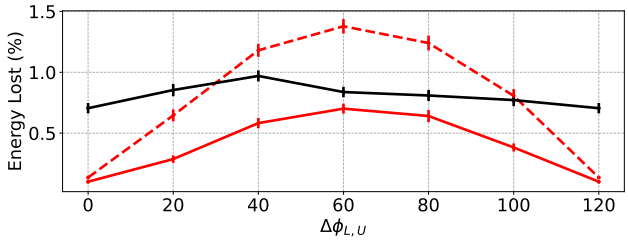

Figure 3: Percentage of alpha-particle energy lost due to the $N = 3$ component only (solid red), $N = 3$ and 6 components combined (solid black), and $N = 3$ with twice the amplitude, which mimics the strength of the $N = 6$, representing the case where an infinite number of ELMcc produces a pure $N = 3$ perturbation (dashed red). The phase of the middle coil set is fixed at $\Delta\phi_M = 0°$, while the phases of both the lower and upper sets vary over one full period, $\Delta\phi_{U,L} = 0°$ to 120°.

about 1% at $\Delta\phi_{U,L} = 40°$. Notably, the energy loss never falls below 0.65%, since even when all current profiles are in phase, the sideband remains out of phase. Therefore, attempts to optimize RMP-induced alpha-particle losses by adjusting the ELM coil phase offer only limited benefits.

In the case of a pure $N = 3$ mode with twice the realistic amplitude, mimicking the combined field strength and plasma penetration of both sidebands ($N = 3$ and $N = 6$) while avoiding phase disagreement between components, the energy lost is negligible when the current profiles of the coil sets are in phase. However, the loss peaks at nearly 1.4% when the coil sets are out of phase. This occurs because the perturbation penetrates deeper into the plasma and can drive alpha-particle transport closer to the core.

This result differs significantly from the deuterium beam losses reported in [24, 27]. The percentage of alpha-particle energy loss is considerably smaller than that of the deuterium beam energy, since alpha-particles are predominantly produced in the core, whereas the deuterium beam undergoes significant ionization throughout the entire plasma column. Furthermore, the toroidal location of the neutral beam injection introduces a new parameter that potentially allow optimization of ELM control strategy. Nevertheless, the overall energy lost by the two species are comparable, resulting in similar potential damage to the PFCs [24, 27, 30, 31].

The remaining sidebands are only significant in the vicinity of the coils and do not penetrate deeply into the plasma. Consequently, their influence on alpha particle transport is minimal, contributing only to minor redistributions of the power flux at the first wall, specifically at locations such as the FILD probe in ITER, similar to the contribution of the TFR. The result containing all sidebands is detailed in section 3.

In any case, the impact on alpha particle transport is negligible and does not vary significantly with the phase configuration adopted. According to references [32, 33], the optimal configuration for ELM mitigation is achieved when the coil current profiles of the upper, middle, and lower coil sets are phased at $\Delta\phi_{U,M,L} = 53.3°, 0°, 73.3°$, respectively, with each set operating at its maximum current amplitude of $I_0 = 90\,\mathrm{kAt}$. This configuration is adopted for the rest of this report.

2.2. Impact of the plasma response on alpha transport

The plasma response to RMPs can significantly alter the characteristics of alpha particle transport [34]. This response decays approximately as $1/N^2$, and is therefore particularly important for components with low toroidal mode numbers, specifically $N \leq 6$. As such, these toroidal harmonics must be treated carefully to account for plasma response effects. MARS-F[35] is a linear code that solves the full resistive MHD equations in the presence of externally applied magnetic fields. The plasma response is modelled‡ using MARS-F, assuming a Prandtl number of 0.3 and a ratio of toroidal momentum to thermal confinement times $\tau_\phi/\tau_E = 2$, as anticipated from turbulent transport simulations for ITER [36, 37, 38].

Among the effects arising from the plasma response, the most important are:

- Shielding of the plasma from external perturbations, which diminishes the absolute value of the perturbation in the plasma core and could potentially reduce transport, especially in highly conductive plasmas.
- Additional perturbations in the upper and lower regions of the plasma poloidal cross-section can potentially increase transport. This effect is particularly significant near the X-point, where the poloidal magnetic field is weaker, causing particles to transit a longer toroidal distance for a given poloidal location. An illustration of these perturbations is shown in figure 4, which depicts

‡ Plasma response computed by Y.Q. Liu and L. Li [32, 33, 36] and available in ITER database

the poloidal distribution of the perturbed radial field of vacuum and plasma response case. The X-point is located approximately at $R = 5.2$ m, $Z = -3.5$ m.

- The self-organising nature of the plasma response repairs the broken magnetic flux surfaces, substantially reducing the stochastic behaviour of the 3D field perturbation and confining stochastic losses to orbits very close to the edge. The effect is illustrated in figure 5.

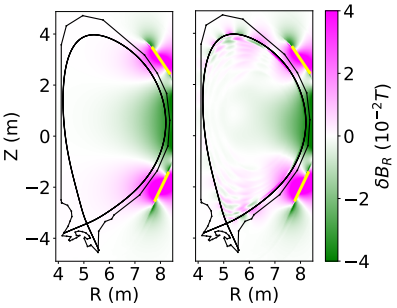

(a) Vacuum (b) P. R.

Figure 4: Illustration of the radial magnetic field perturbation comparing the vacuum approximation (a) with the case including the plasma response (b). Field at $\phi = 71^o$, that maximizes the different between field produced by upper and lower set to the middle set, for better illustration.

To obtain good resolution for all characteristic orbits, the number of markers is increased to one million. Figure 5 compares the Poincaré plots of the 3D magnetic field and the corresponding impact on transport, based on the initial conditions of the alpha particles after the D-T reaction. The comparison is made with respect to the pitch angle ($v_\parallel/v^\star$, $\parallel$ to the magnetic field) and the magnetic surface ($\psi_N^\star$) where the alpha orbit intersects the outer mid-plane. As trapped particles cross the outer mid-plane twice, they are represented by negative/positive $v_\parallel/v^\star$ if born in counter/co-moving sections of banana orbit, respectively, and $\psi_N^\star$ corresponds to the inner/outer part of their banana orbit crossing the mid-plane, respectively.

The observed asymmetry between negative and positive pitch angles for passing particles in figure 5 is attributed to their orbit widths which drifts toward either the high-field or low-field side for counter or co-passing ions. A similar asymmetry is observed for trapped particles, given by the poor confinement of particles born in the inner portion of the banana orbit, close to plasma edge, counter travelling the magnetic field.

Passing particles follow the magnetic field lines closely and are therefore strongly subject to stochastic transport. Consequently, the plasma response dramatically mitigates passing particle transport by reducing the stochasticity of the magnetic field [34, 30], as in figure 5. The energy lost in the vacuum case is

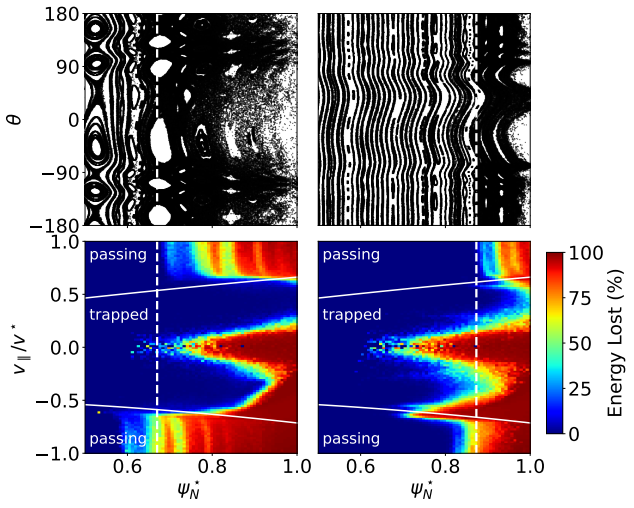

(a) Vacuum (b) P. R.

Figure 5: Poincaré plots (*upper*) and maps of the percentage of alpha-particle energy lost due to RMPs (*lower*) in vacuum (a) and with plasma response (P.R.) (b). The axes in the figure represent pitch angle $v_\parallel/v^\star_{\rm tot}$ and magnetic surface $\psi_N^\star$ for an alpha particle initial orbits at the point where they cross the outer mid-plane. Solid white lines indicate the boundary between passing and trapped orbits, while the dashed white line shows the penetration of the stochastic region.

dominated by passing particle losses, thus, the plasma response reduces the overall losses.

On the other hand, the plasma response enhances trapped particle transport [34, 30] by two distinct mechanisms. First, the introduced poloidally extended perturbations give rise to a new source of transport channel for the trapped particles with their turning points near the X-point, represented by $v_\parallel/v^\star_{tot} \approx -0.5$. Secondly, the deeply trapped orbits ($|v_\parallel/v^\star_{tot}| \leq 0.3$) experience increased transport due to the narrowing of the distance between the upper and lower perturbation around the mid-plane (the magenta areas are slightly closer together in the plasma response case, figure 4), which increases the effective phase differences between the three sets of coils experienced by particles in deeply trapped orbits close to mid-plane.

The overall results are in qualitative agreement with ASCOT [34]. However, a slightly different effect is observed at the boundary between trapped and passing particles. LOCUST predicts that the plasma response mitigates transport in this boundary region, whereas ASCOT predicts an enhancement of transport. This discrepancy is most likely due to the guiding-centre approximation [25, 14] employed in ASCOT to accelerate simulations, while LOCUST uses full orbit calculations throughout the entire slowing down time. The scale length of the plasma response perturbed field is of the same order of the alpha particle Larmor radius ($\sim$ 5 cm), where the guiding-centre approximation may face limitations.

The discrepancy has a minor effect when comparing the overall losses. On the other hand, this region is

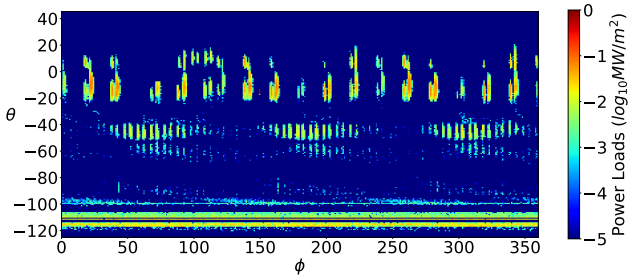

Figure 6: Overall view power flux density, discriminated by the poloidal angle θ and toroidal angle ϕ.

responsible for energy deposition in the cooling pipes beneath the divertor dome, structures with complex geometry that can concentrate the power flux and must be protected from damage. These structures are significantly better protected if the particles are followed in full orbit instead of guide centre [34].

The effect of the plasma response on particle transport close to the trapped/passing boundary remains an open topic, as the physics of the plasma response is not yet fully understood, and alternative methods of calculating this response can yield differing results.

3. Localized power flux

To accurately calculate the power flux on the PFCs, LOCUST first tracks the orbits of one million markers representing alpha particles, from their production in the D–T reaction until they collide with the PFCs or thermalize. An overall view of the power loads is illustrated in figure 6.

The power loads exhibit the main toroidal mode number $N = 3$ with the $N = 6$ sideband footprint on the outer wall ($\theta \geq -80°$) and, less prominent on divertor regions ($\theta < -80°$). The component $N = 18$ from the TF-ripple is also visible together with the protuberances of the PFCs around $\theta \sim -10°$. Figures 7a, 7b and 7c shows the protuberances. The remaining sidebands contribute to minor redistribution.

To accurately calculate the power flux density in detailed structures, LOCUST track the orbits again, employing a specialised resampling technique [25]. This resampling method utilises the state of the markers that were lost among the one million initial markers, 0.1 to 0.2 ms before they impact any PFC and tracking the markers again for a very short duration. As a result, the markers follow different paths due to Monte Carlo collisions and strike the PFCs at different positions, reducing peaks in power flux that arise from a small number of markers deposited on the surface. The technique is detailed in appendix 1. The power flux density maps of the relevant PFCs are presented in figures 7.

Table 1 list the values of the absolute energy deposited in each ITER component (divertor components listed in figure 8) and the respective peak power flux to which the components are exposed, for the vacuum case and with plasma response included, respectively.

The cooling pipes under the dome must be protected and deserve attention. Due to their complex morphology, shown in figure 7e, the power flux concentrate on the front edge of each pipe. Furthermore, the dome divertor consists of several blocks, with gaps between each block, creating a special situation where the first pipe of each set receives an additional power load, nearly double that of the other pipes, consistent with a missing pipe between each set. This behaviour was previously observed for deuterium beam fast ions transported by static 3D fields [24, 25]. It is reasonable to expect similar behaviour for loads arising from other sources of transport, such as TAE, fishbones, etc. All these transport mechanisms should be collectively calculated to assess the final impact.

The total power deposited on the cooling pipes is found to be 13 kW, with a maximum power flux density of 0.25 MW/m^2 in the plasma response case. This figure is comparable to expected levels of thermal and radioactive loads, thus ensures safe operation. Furthermore, the value is 50% smaller than that obtained in the vacuum approximation case, thus the plasma response plays an important role.

Previous studies using guide-centre orbit following [34] reported that the plasma response increases the overall power on the cooling pipes by nearly 10%, due to enhanced transport in the passing/trapped boundary. Moreover, the previous calculations predicted an overall power to the pipes on the order of 120 kW, nearly ten times the value calculated herein. This discrepancy in absolute values arises from ASCOT not employing a detailed description of divertor structures, which leads to an overestimation of alpha particles transported towards approximated locations corresponding to the cooling pipes.

The power flux on the cooling pipes arises from particles in the trapped–passing boundary region. This special condition makes it sensitive to the orbit-following technique and potentially sensitive to the plasma response model. Perturbations around the X-point also play a crucial role in redirecting power towards different divertor components. It is important to note that the MARS-F plasma response model used in this study is limited and does not incorporate a realistic X-point geometry. Plasma response modelling remains an open research topic, particularly relevant for protecting vulnerable structures in future devices, such as the ITER cooling pipes located under the dome.

4. Fast Ion Loss Detector

The Fast Ion Loss Detector (FILD) [18] is a key diagnostic instrument designed to monitor dynamics of energetic particle losses in fusion plasmas and plays a crucial role in validating theoretical models and enhancing our understanding of fast ion behaviour under the influence of various perturbations [21]. The FILD is a probe designed to intercept the trajectories

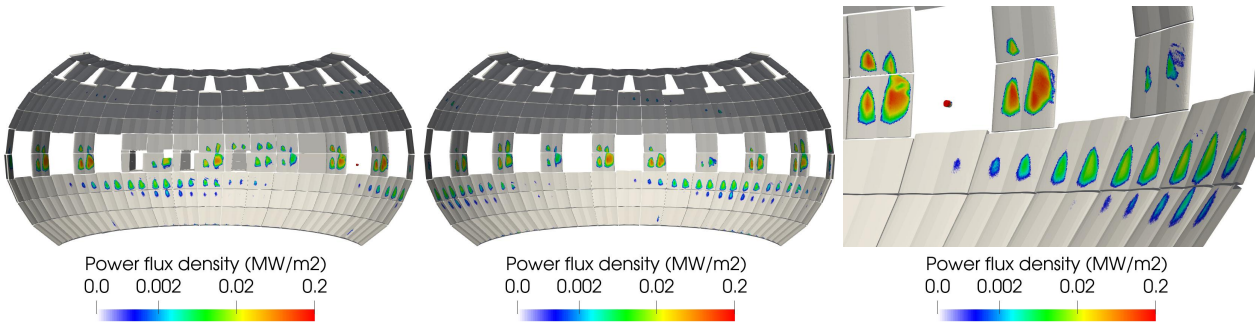

(a) Wall, $0^o \leq \phi < 180^o$ (b) Wall, $180^o \leq \phi < 360^o$ (c) Wall around FILD

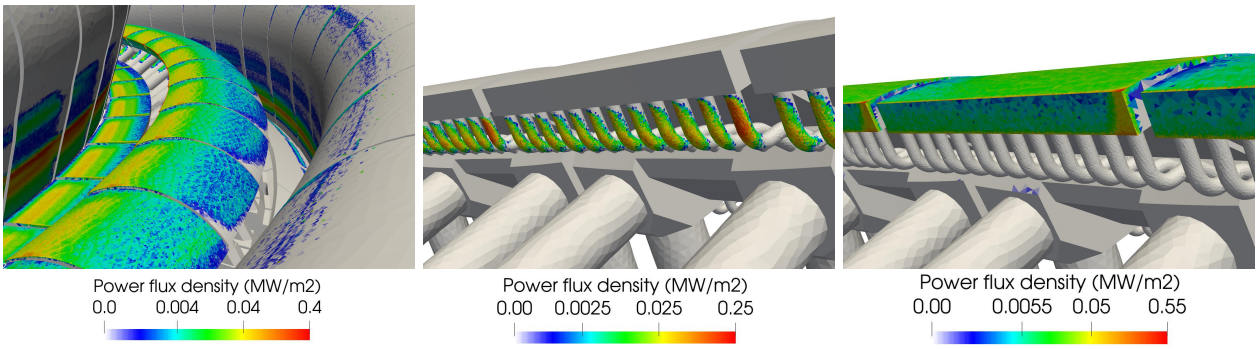

(d) Divertor (e) Cooling Pipes (f) Dome divertor

Figure 7: Power load distributions across different PFCs; a) first wall for $0^o \leq \phi < 180^o$, b) first wall for $180^o \leq \phi < 360^o$, c) first wall in the vicinity of the FILD (red dot on the equator port), d) overall divertor structures, e) inner cooling pipes under the dome divertor and f) corner of dome divertor.

	Vacuum case		Plasma Response case	
Component	Power (kW)	Max. flux (MW/m^2)	Power (kW)	Max. flux (MW/m^2)
First Wall	76 ± 2	0.12 ± 0.02	220 ± 3	0.20 ± 0.03
Inner Div. Target	446 ± 5	0.58 ± 0.03	97 ± 2	0.40 ± 0.03
Inner Baffle	424 ± 5	1.30 ± 0.07	146 ± 3	0.29 ± 0.07
Inner Dome Div. Sup.	13 ± 1	0.18 ± 0.03	9 ± 1	0.16 ± 0.03
Over Dome Div.	223 ± 3	0.70 ± 0.03	184 ± 3	0.55 ± 0.03
Outer Div. Target	0.8 ± 0.1	0.02 ± 0.01	0.8 ± 0.1	0.03 ± 0.01
Outer Baffle	834 ± 9	0.85 ± 0.03	140 ± 5	0.30 ± 0.03
Inner Cooling Pipes	26 ± 1	0.42 ± 0.09	13 ± 1	0.25 ± 0.08

Table 1: Overall power and peak of power flux density on each component in the vacuum case and plasma response case.

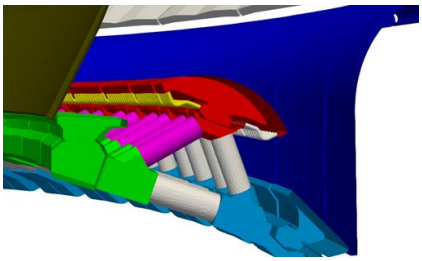

Figure 8: Identification of divertor PFCs: dark green - Inner Baffle, light green - Inner Div. Target, pink - Inner Dome Div. Support, yellow - Inner cooling pipes, red - Over Dome Div., light blue - Outer Div. Target and dark blue - Outer Baffle.

of energetic particles outside the confined region and prior collision with the tokamak PFCs.

It features a small pinhole which fast particles pass through, followed by a collimator that selects particles within a specific range of gyro-phases. Particles passing through the pinhole and collimator system subsequently strike a scintillant plate, where their Larmor radii and pitch angles determine the impact locations. The resulting photon emission is then captured by a camera [18].

An alpha particle and a deuterium beam ion (or any other fast ion) with the same pitch angle and Larmor radius will strike the same location on the scintillant plate regardless of their differences in mass and energy. However, as only alphas are included in the results, to facilitate the interpretation, the fast ion distributions of lost particles are presented as spectrograms of energy and pitch angle.

The pinhole/collimator system directly affects

both the flux of fast particles reaching the scintillant plate and the resolution of the strike map. A more restrictive system improves the resolution but reduces the fast particle flux, potentially dropping it below the noise level. One of the main challenges in the design of the FILD probe is to optimise the geometry of the pinhole and collimator such that sufficient alpha-particle flux reaches the scintillant plate to ensure a detectable signal, whilst maintaining adequate resolution [20]. This section presents high-fidelity simulations predicting the alpha-particle flux on the FILD probe and scintillant plate, supporting the design and optimisation of the ITER FILD system.

4.1. FILD position

The ITER FILD will be capable of radial movement, allowing adjustment of the distance between the probe and the LCFS in order to optimise particle flux detection under varying plasma conditions. The analysis below presents the operational range of radial positions in which the FILD can function as an alpha particle loss diagnostic for the ITER baseline scenario.

The radial position of the FILD pinhole is denoted as R_{pin}, and serves as the key parameter describing the FILD location. The useful operational range is determined by two criteria: the lower limit is set by the R_{pin} at which the alpha-particle flux is sufficient to be detected above the noise level, while the other limit corresponds to the R_{pin} beyond which the peak of the power flux density exceeds the FILD design threshold of 10 MW/m^2 in any part of the probe.

Although the density in the scrape-off layer (SOL) is low, tempting one to neglect its effects, the low temperature accelerates the slowing-down process compared to core plasma conditions. This makes uncertainties in the SOL potentially significant for the heat flux on the probe and the resulting fast ion distribution. In fact, increased SOL density can have a protective effect on heat loads from deuterium beam ions to PFCs [25].

To address uncertainties related to the SOL density, two extreme cases are considered: one neglecting the SOL density, denoted as vacuum SOL, and another extending the LCFS profiles to near the first wall, representing a scenario with much elevated density values.

The overall power deposited on the probe and the corresponding peak power flux density are shown in figure 9.

The LCFS is located at approximately $R \approx 8.2\,\text{m}$, and the alpha-particle flux increases as the FILD approaches this position.

When the FILD is positioned at $R_{\text{pin}} = 8.30\,\text{m}$, it operates near the threshold of its design limits. Although the peak alpha-induced power flux at this position is approximately $7.7\,\text{MW/m}^2$, the inclusion of additional sources, such as deuterium beam injection and uncertainties in the scrape-off layer (SOL) density may raise the peak of power flux beyond the $10\,\text{MW/m}^2$ threshold. This establishes the high-flux

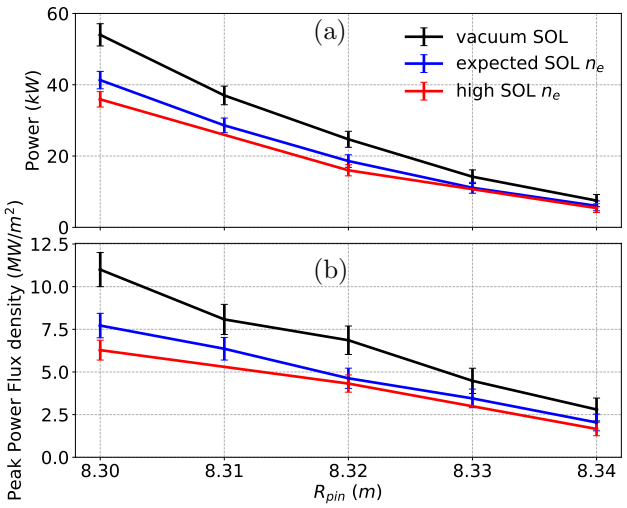

Figure 9: Graphic displays the total energy deposited (a) and the peak power flux density (b) on the FILD, at different radial positions.

operational limit near $R_{\text{pin}} = 8.31\,\text{m}$.

The FILD is located in an equatorial port, as shown in figure 7c. The protrusions of the outer wall approaching the plasma, at the vertical position of the FILD, are situated at approximately $R \approx 8.34\,\text{m}$. Figure 10 illustrates the power load flux density maps for different radial positions of the FILD. The wireframe in figure 10 marks the surface corresponding to the protuberances of the first wall, beyond this radial location, the power flux rapidly decreases due to absorption by the first wall.

As shown in figure 10, at the wireframe, the power flux density reaches around $0.5\,\text{MW/m}^2$. This value is of the same order of magnitude as the peak power flux on the first wall; $\sim 0.2\,\text{MW/m}^2$, see Table 1. When the FILD is positioned at $R_{\text{pin}} = 8.34\,\text{m}$, the power flux density near the pinhole (figure 13) is also approximately $0.5\,\text{MW/m}^2$.

Furthermore, at locations $R > 8.34\,\text{m}$, beyond the wireframe shown in figure 10, the alpha flux rapidly diminishes. This region lies at a radial position further away from the LCFS than the nearby PFCs, thus shielded by the first wall protuberances. Positioning the FILD at $R_{\text{pin}} > 8.34\,\text{m}$ significantly limits its ability to capture sufficient flux across a broad range of particle orbits. This establishes the low-flux operational limit near $R_{\text{pin}} \approx 8.34\,\text{m}$.

The fast ion distribution impacting the entire probe at each radial position is shown in figure 11. The 2D coloured histogram represents the alpha flux on the probe, discriminated in terms of energy and pitch angle ($v_\parallel/v$).

The fast ion distribution is predominantly composed of trapped alpha particles, which can be qualitatively categorized into two distinct orbit types: deeply trapped banana orbits, located approximately within the region where $v_\parallel/v < 0.5$, and broad banana orbits, corresponding to $0.5 \leq v_\parallel/v < 0.7$, whose turning points are situated near the X-point. Additionally, a

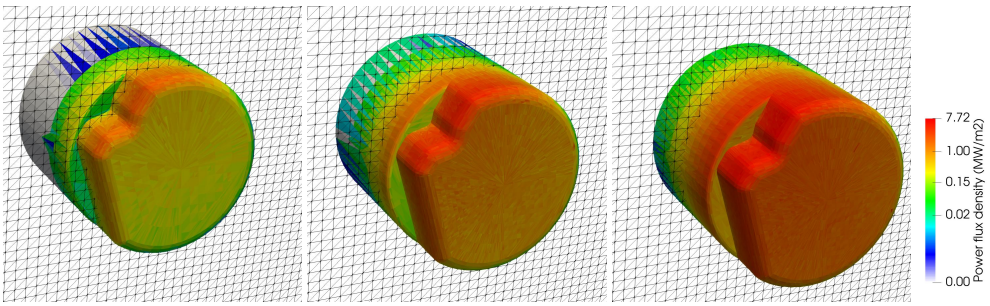

(a) $R_{pin} = 8.34$m (b) $R_{pin} = 8.32$m (c) $R_{pin} = 8.30$m

Figure 10: Power flux density maps on the probe at different radial positions. The wireframe represents the surface corresponding to the protuberances of the first wall closest to the plasma, at the vertical location of the FILD. The maps represents the expected SOL density case.

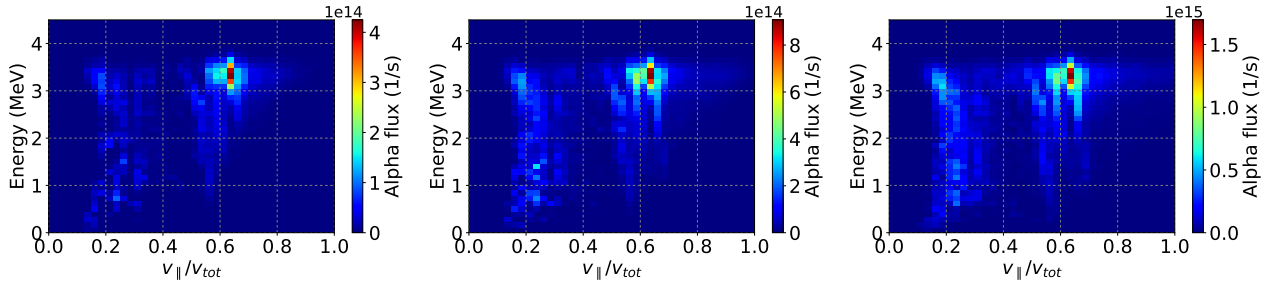

(a) $R_{pin} = 8.34$m (b) $R_{pin} = 8.32$m (c) $R_{pin} = 8.30$m

Figure 11: Fast ion distributions on the entire FILD probe at various FILD positions.

residual tail of passing particles with $v_\parallel/v \geq 0.7$ affects the FILD as it moves closer to the plasma.

The deeply trapped orbits correspond to alpha particles that bounce within a narrow poloidal region and are therefore exposed only to highly localized sources of transport. Nevertheless, they contribute significantly to the heat load on the front edge of the probe, thereby playing a critical role in constraining the range of permissible operational positions.

The broad banana orbits region consists predominantly of particles born in the inner half of the banana orbit, counter-passing the magnetic field. As to the observed asymmetry between negative and positive pitch angles of trapped particles, shown in figure 5. Moreover, since the inner half of these orbits penetrates deeper into the plasma, they are exposed to additional transport mechanisms during the short time window prior to being captured by the FILD. Given their access to the regions relatively closer to the plasma core, these orbits are of particular interest for assessing transport processes and are thus among the most valuable to register with the FILD.

Passing particles closely follow magnetic field lines, exhibiting lower drift and smaller Larmor radii, with their outermost points of their orbits located nearer the LCFS. These particles tends to affect the divertor region.

As the FILD moves radially inward and approaches the plasma, it transitions from functioning as an extension of the first wall to acting as wide range alpha diagnostic, capable of capturing particles that impacts the divertor. Passing particles that move away from the LCFS in the outer mid-plane (i.e. with significant orbit drift toward the low-field side, thus lower pitch angle, higher Larmor radius and closer to trapped boundary), may thus potentially be detected. However, moving the FILD closer to the plasma also increases the heat flux on the probe, thereby constraining the operational range of the FILD. Within the permitted range of operation, the flux of passing particles may unfortunately remain below the noise threshold in the RMP-induced alpha losses investigations.

Figure 12 illustrates the influence of uncertainties in the SOL density on the diagnostic performance, it presents the fast ion distributions of alpha particles impacting the entire FILD probe for the considered density scenarios.

Despite significant differences between the SOL density profiles, the impact on orbits with $v_\parallel/v \geq 0.5$ is negligible. This indicates that the alpha-particle populations of greatest interest are not affected by variations in the SOL density.

On the other hand, the flux of orbits with $v_\parallel/v < 0.5$ decreases as the density in the SOL increases. These orbits remain confined near the SOL for a long period before striking the FILD, resulting in non negligible absorption within the SOL. Additionally, collisional transport can redirect these particles toward the first wall. This effect is particularly pronounced at lower energies, as the likelihood of thermalization or wall absorption prior to detection by the FILD increases.

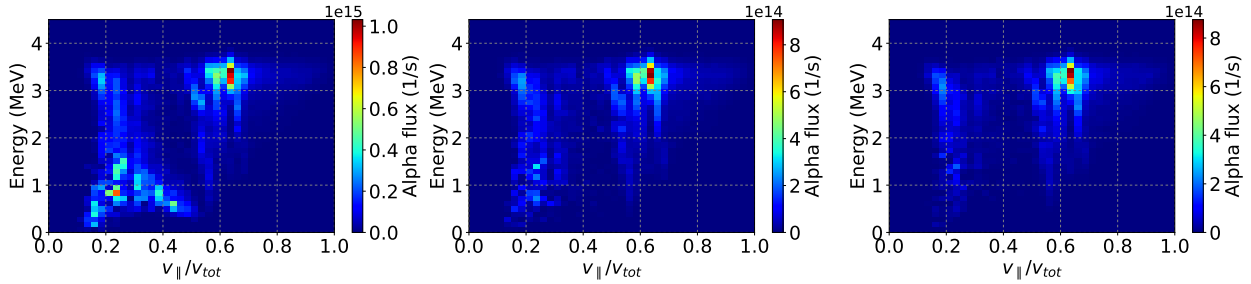

(a) Vacuum SOL (b) Expected SOL density (c) High SOL density

Figure 12: Fast ion distributions of alpha particles impacting the entire FILD probe for different SOL density profiles, with the FILD positioned at $R_{\text{pin}} = 8.32\,\text{m}$.

The majority of collisions involving alpha particles occur with electrons. The transport saturates before alpha-ion interactions become predominant. Furthermore, other sources of equilibrium profiles, such as deuterium, tritium, and impurity densities, have a lesser impact on the results. Only helium ash is included in the simulation; the results are for 10% of helium ash, and a scan varying its concentration from 0 to 20% of the ion density found its influence to be indistinguishable.

Recent modifications to the ITER wall materials, particularly the introduction of tungsten, have raised concerns regarding tungsten impurities. Nevertheless, within the scope of alpha-particle transport under static 3D magnetic field perturbations, the influence of tungsten impurities is anticipated to be primarily indirect, acting through its impact on the electron density profile.

It is important to note that the MARS-F plasma response model employed herein does not incorporate a realistic X-point or scrape-off layer (SOL), which limits its accuracy, particularly near the LCFS. Consequently, uncertainties in the plasma response may affect different regions of the fast ion distribution to varying degrees. Specifically, the inaccurate representation of the SOL is expected to have a greater impact on deeply trapped orbits, whereas limitations near the X-point may influence broader trapped orbits and, to some extent, passing orbits as well.

Finally, despite the possible uncertainties in the profiles and limitations of the plasma response model, these factors have minimal impact on the applicability of the present results to the design of the FILD pinhole and collimator. The FILD position remains a free parameter that can be adjusted to optimize the balance between the maximum power flux density on the probe and the alpha flux at the pinhole, a relationship that is expected to be consistent with the current simulations.

4.2. Estimating alpha flux passing through the pinhole and collimator

To produce a synthetic diagnostic, it is necessary to estimate the alpha flux in each interval of energy and pitch angle passing through the pinhole, as illustrated in figure 13.

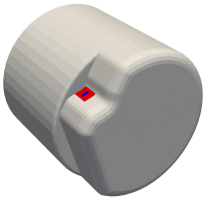

Figure 13: Illustration of the FILD showing the pinhole highlighted in blue, with the surrounding region indicated in red.

Several approaches can be used to estimate the alpha flux on the pinhole. Figure 14 illustrates how the choice of area considered affects the results. Figure 14 a) shows the total flux over the entire probe divided by the affected area, i.e., all regions of the FILD probe where alphas are deposited. Figure 14 b) restricts the area to a small region surrounding the pinhole, corresponding to the red area in figure 13. Figure 14 b) further limits the area to the pinhole itself, shown as the blue region in figure 13.

Considering all alpha particles impacting the FILD, as shown in figure 14 a), result in very small uncertainties but underestimates the flux at the pinhole by a factor of up to 4. This discrepancy arises because the flux is not homogeneously distributed across the probe surface but concentrates near the edge where the pinhole is located. As a result, the signal of the synthetic diagnostic in the next section of this work is significantly higher than previously reported by ASCOT [19], which method approaches the one used in figure 14 a), comparing cases with a similar range of alpha flux over the entire probe, potentially impacting the FILD design.

Figures 14 b) and 14 c) present consistent flux values, as the flux distribution is more homogeneous over these smaller and overlapped areas. However, the error bars increase rapidly as the considered area decreases, due to the limited number of samples within the restricted pinhole region. Consequently, the area surrounding the pinhole is used to provide a clear and reliable estimate of the flux passing through the pinhole, since it shows good agreement with the flux directly on the pinhole itself.

The pinhole is oriented in a plane defined by the

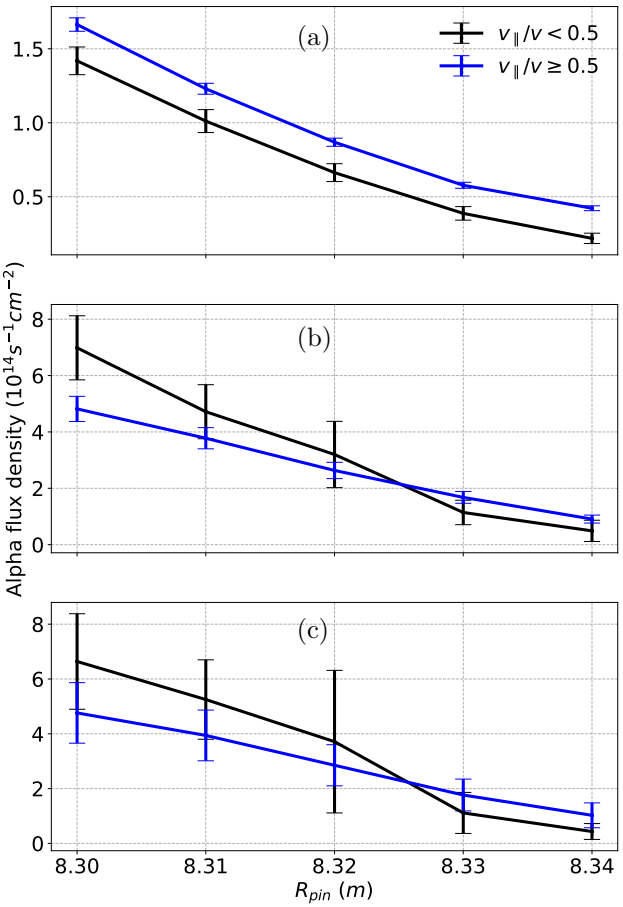

Figure 14: Estimation of the alpha flux density at the pinhole considering three different areas; (a) shows the total flux over the entire probe divided by the affected area, (b) shows the alpha flux density in a small region surrounding the pinhole, indicated by the red area in figure 13, and (c) shows the alpha flux density restricted to the pinhole area itself, shown as the blue area in figure 13.

magnetic field direction ($B_R \approx 0$, $B_\phi = -4.1$, $B_Z = 1.3$) and the radial direction. To enhance the resolution of the scintillant plate strike map, the collimator restricts the acceptance to a narrow range of gyro-phases of the incident particles.

The range of selected alpha particles can be described by the so called incident gyro-phase (ϑ), defined as the component of the incident angle perpendicular to the magnetic field of the alpha particles passing through the pinhole, and thus perpendicular to the plane in which the pinhole is located. Positive values of ϑ corresponds to particles with positive radial velocity (upper side of the gyro-orbit).

Two approaches can be used to estimate the fraction of alpha particles able to pass through the collimator. The first approach conservatively assumes a homogeneous distribution of gyro-phases, while the second relies on analysing the results in the area surrounding the pinhole. The second, and more accurate, method requires a sufficient number of markers qualitatively equivalent to those passing through the pinhole, thereby reducing statistical error. This is only feasible by the techniques used herein and described in the Appendix 1. Figure 15 illustrates these approaches.

The distribution of the incident angle can be explained by two main reasons: Firstly, for a small movement along the gyro-orbit, the particle travels a distance proportional to $\cos\vartheta$ relative to the plane in which the pinhole is located, increasing the likelihood of a particle cross the plane when the particle presents perpendicular movement ($\vartheta = 0$). Secondly, the negative radial density gradient of the available energetic particles enhances the distribution around $\vartheta \sim 0$, simply by capturing more particles travelling closer to the plasma, which are near the outermost region of their gyro-orbit. To illustrate this situation, we assume a homogeneous gyro-phase distribution of the available alphas in each magnetic surface located at the guiding-centre orbit and constant and strong radial density gradient, the effect also scales with $\cos\vartheta$, corresponding to the radial (horizontal) distance between the pinhole and the position of the guiding-centre orbit of these particles (which is the Larmor radius multiplied by $\cos\vartheta$),

The estimated distribution in figure 15 ($\propto \cos^2\vartheta$), shows fair agreement with the simulation results, particularly at $R_{pin} = 8.30$m, figure 15c, where the FILD is located closer to the plasma and farthest from the first wall, thus less influenced by the protuberances nearby. The peak of the distribution obtained in LOCUST shifts from 0 to negative ϑ due to the asymmetry in the FILD position relative to the magnetic axis ($Z_{\mathrm{FILD}} \approx 9\,\mathrm{cm}$ and $Z_{\mathrm{mag}} \approx 60\,\mathrm{cm}$), as well as the protuberances on the first wall, see figure 7c or at $(\theta, \phi) \approx (-40/180)^\circ$ in figure 6. The flux within the range permitted by the collimator is nearly twice the conservative estimation.

It is not possible to generalise a estimated distribution function that applies universally, due to the influence of the first wall. An accurate estimation must therefore be obtained through an orbit-following code that employs a realistic geometry of the PFCs on the first wall and follows the particle in full-orbit throughout at least the last few μs before the particle hits any PFC, and with a sufficient number of markers representing the alpha particles. In any case, the alpha flux peaks close to the collimator acceptance range and exceeds the conservative estimate by approximately a factor of approximately 2 in the cases examined herein.

Finally, considering a factor of 4 arising from the choice of the analysed area on the FILD, along with an additional factor of 2 due to a more accurate estimation of the incident gyro-phase distribution, the flux passing through the pinhole/collimator system can be underestimated by up to a factor of 8.

4.3. Synthetic diagnostic - Scintillant plate

After passing through the pinhole and the collimator, the alpha particles strike the scintillator. The finite

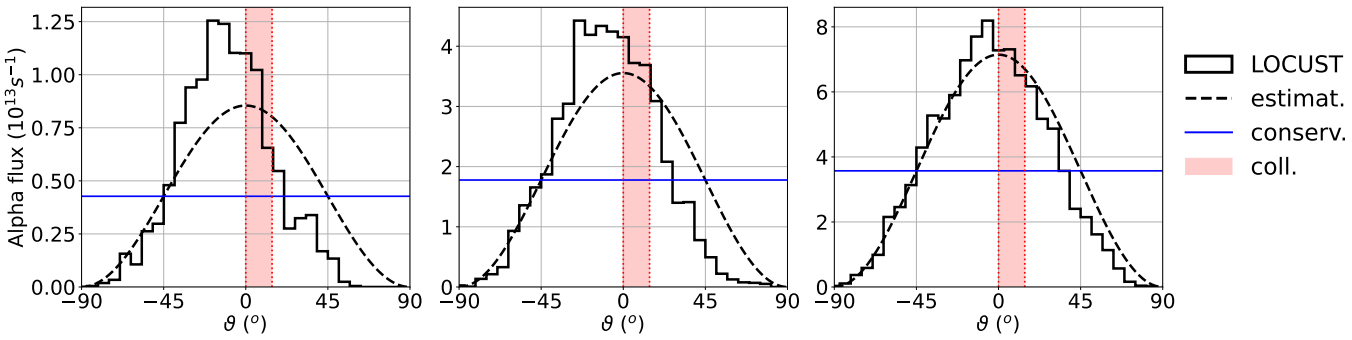

(a) $R_{pin} = 8.34$m (b) $R_{pin} = 8.32$m (c) $R_{pin} = 8.30$m

Figure 15: Illustration of the ϑ distribution of the alpha flux at the pinhole. The solid black line represents the ϑ distribution obtained from LOCUST simulations, the dashed black line shows a estimated distribution function, and the blue line corresponds to the conservative estimation. The red area indicates the limits of the gyro-phases that pass through the collimator.

size of the pinhole, along with the range of incident angles permitted by the collimator, directly affects the resolution of the strike point on the scintillator's surface.

FILDSIM [28, 39, 40, 41] produces high-quality synthetic diagnostics and has been validated against experiments [42, 43, 44, 14]. It accounts for uncertainties introduced by the finite dimensions of a realistic three-dimensional description of the pinhole and collimator, based on the actual planned ITER-FILD design. The samples recorded in the region surrounding the pinhole are resampled at random locations within the pinhole's boundaries. The gyro-phase distribution of the resampled markers is then determined by the collimator design [39], assuming the conservative (uniform) distribution of gyro-phases on the pinhole and the realistic geometry of the collimator. The orbits of the resampled markers are subsequently projected onto the scintillator.

A more accurate simulation requires rescaling the resampled gyro-phase distribution so that it is consistent with the results obtained with LOCUST. The flux on the scintillator should increase, as the gyro-phase distribution within the collimator-permitted range is higher than the conservative assumptions. Some distortions may also appear, as the distribution is no longer uniform across the collimator's acceptance. This distortion can be significant, especially for positions where $R_{\rm pin} > 8.32\,$m, when nearby protuberances of the first wall impact the diagnostic signal. The gyro-phase dependant collimator factor will be included in the next FILDSIM update release.

Figure 16 presents the FILD synthetic diagnostic of alpha losses in the baseline scenario. The plot illustrates the patterns of alpha flux density on the scintillant plate for FILD positions ranging from $R_{\rm pin} = 8.34,$m to $8.31,$m.

The broader orbits presents two maxima, at $v_\parallel/v \sim 0.58$ and $v_\parallel/v \sim 0.64$. Approaching the plasma strongly enhances the definition of the $v_\parallel/v \sim 0.58$ peak, capturing it prior being absorbed by the first wall. These two peaks presents a distinguished resonance conditions and returning points, thus it is an advantage to be able to identify then both. For $R_{\rm pin} \leq 8.32\,$m, the peak presents a flux with a maximum of 2.0×10^{15}s^{-1}m^{-2} separate by a minimum of 1.0×10^{15}s^{-1}cm^{-2}. A third broad orbit maximum is observed near $v_\parallel/v \sim 0.53$ when the FILD further approaches the plasma. The broader orbit losses correspond to alphas near the birth energy.

The flux associated with deeply trapped orbits, characterised by $v_\parallel/v \leq 0.5$, rapidly increases when $R_{\rm pin} \leq 8.32\,$m, capturing alpha particles with multiple energies.

The isolated maxima observed in the region of small energies ($\leq$ 1 MeV) arises from insufficient statistical accuracy due to a limited number of markers in this specific regions of the strike map and do not represent a significant result. The focus of this study is to characterise the physics of alpha particles, and this area of the strike map may overlap with the flux of deuterium beam ions, making the individual contributions indistinguishable. As such, a detailed analysis of this region lies beyond the scope of the present paper.

Overall, the optimal position is identified at approximately $R_{\rm pin} = 8.32\,$m, where a clear signal is observed across two distinct broad orbit populations, along with appreciable levels of deeply trapped orbits, while simultaneously avoiding excessive heat loads on the probe.

Maximizing the signal in the scintillator is essential to ensure that all relevant phenomena are seen. Capturing alpha flux as low as $0.5 \times 10^{15}\,$s$^{-1}\,$m^{-2} and a saturation level of at least $2.0 \times 10^{15}\,$s$^{-1}\,$m^{-2}, is sufficiency to register all maxima separately.

Excessive power flux density can potentially damage the FILD scintillator, especially with long time exposure. The peak of power flux density on the scintillant plate is found to be approximately $0.14\,$W/cm^2 on $R_{\rm pin} = 8.32\,$m, rising to $0.18\,$W/cm^2 on $R_{\rm pin} = 8.31\,$m, and should be within the design limits. Figure 17 presents the power flux density on the scintillant plate, for the optimum FILD position.

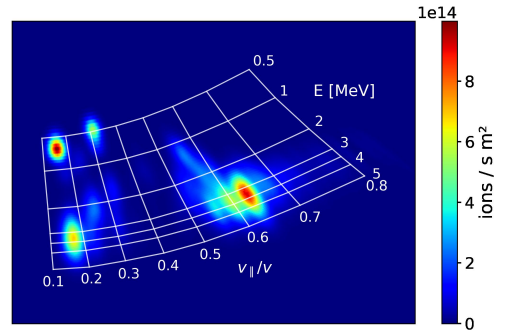

(a) $R_{pin} = 8.34$m

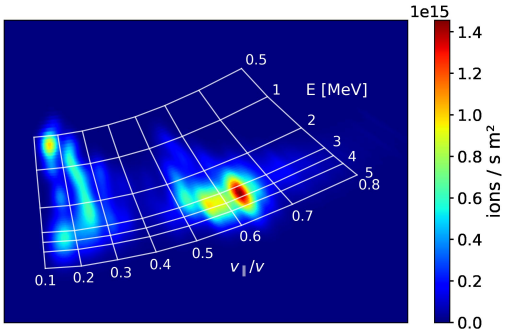

(b) $R_{pin} = 8.33$m

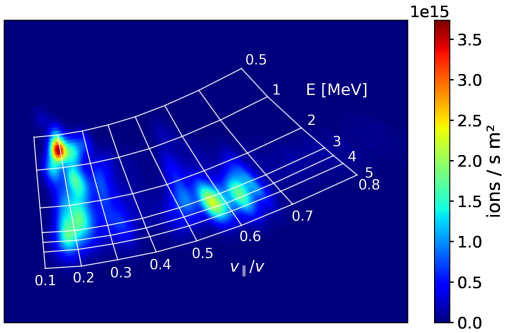

(c) $R_{pin} = 8.32$m

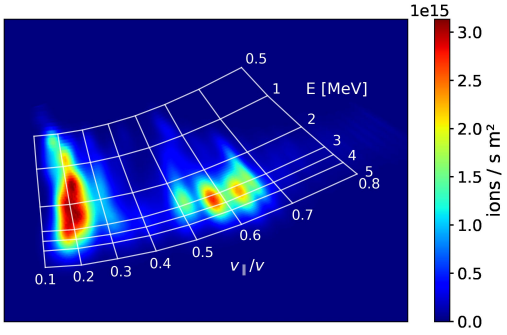

(d) $R_{pin} = 8.31$m

Figure 16: FILDSIM synthetic diagnostics, employing the realistic pinhole and collimator of the current ITER FILD design, based on the LOCUST alpha flux recorded in a small area ($\sim 1\text{cm}^{-2}$) around the pinhole and the conservative, homogeneous incident gyro-phase distribution. The FILD positions are $R_{\text{pin}} = 8.34$ m to 8.31 m. Note that the colourbar scales differ between figures.

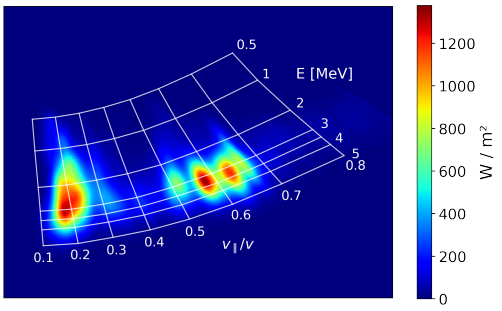

Figure 17: Power flux density on the scintillator plate, relative to the optimal position case, $R_{\text{pin}} = 8.32$ m.

The values of alpha and power flux density on the scintillator plate could potentially increase due to non-uniform distribution of the incident gyro-phase which concentrates around the collimator acceptance range is higher than the conservative estimation adopted in FILDSIM. To reduce the power flux on the scintillator plate, given engineering constraints, it is necessary to either decrease the pinhole size or adopt a more restrictive collimator.

5. Conclusion

The alpha energy lost due to the ELM mitigation strategy is found to be approximately 1% of the total alpha energy produced in the D-T fusion reaction. While optimizing ELM control to improve alpha confinement yields limited benefit, mainly due to sidebands arising from the finite number of coils per set. Nevertheless, the resulting impact on overall alpha heating performance is negligible and the maximums of power flux densities across ITER components remain well below design limits.

Simulation results show qualitative agreement with previous ASCOT studies [34]. The fields arising from the plasma response to the RMPs suppress the magnetic field stochasticity, mitigating the overall alpha transport by reducing passing particle losses. Conversely, trapped particle losses are enhanced by poloidally extended perturbations. The trapped/passing boundary region reveals a discrepancy: LOCUST predicts transport mitigation, while ASCOT indicates an enhancement. This difference likely arises from ASCOT's guiding-centre approximation, which becomes less accurate when perturbation scales approach the alpha particle Larmor radius. LOCUST's full-orbit treatment offers improved fidelity. This issue affect sensitive structures like the unprotected cooling pipes beneath the divertor dome.

In the plasma response case, power deposition on these pipes reaches 13 kW, with a peak flux density of 0.25 MW/m^2, comparable to thermal and radiative loads. It represents a 50% reduction relative to the vacuum case and an order of magnitude in comparison to the previous estimations [34].

The plasma response to externally applied perturbations, especially near the X-point, significantly influ-

ence power redistribution across PFCs. The MARS-F model used here is a linear code lacking realistic X-point representation. Plasma response modelling remains an open area of research, with particular interest for safeguarding critical structures in future devices.

The FILD is intended to operate across various scenarios, including measurements of ion populations heated by cyclotron resonance and neutral beams, as well as low-alpha-power phases. Thus, the probe needs be be accurately designed to fulfil this wide range of purpose. To monitor alpha losses in the flat-top baseline scenario, it needs to approach the plasma and withstand to high levels of power flux on the probe and on the scintillator, therefore, and accurate simulation must be part of the design process.

LOCUST has demonstrated a strong capability in estimating the alpha flux impacting the FILD, providing sufficient detail to accurately determine the alpha flux at the FILD pinhole, highlighting its potential as a tool to support the design of fast ion diagnostics in future devices. The synthetic diagnostic produced by FILDSIM shows that the signal shall be well above the noise level and multiple orbits of interest can be distinguished.

Conservative approaches may significantly underestimate the alpha flux. A factor of nearly 4 can arise from the non-uniform distribution of the alpha flux on the probe, consequently, the localized flux reported in this study is notably higher than previously reported in reference [19]. Moreover, the non-uniform gyro-phase distribution of the samples recorded on the FILD pinhole can further increase the flux on the scintillant plate by a factor of approximately 2. A FILDSIM upgrade is under development to incorporate this feature and the results will be published in the future. This finding has important implications for the ITER FILD design and for future machines with large energetic particle populations.

6. Acknowledgements

This work was funded by UKAEA, the ITER Organisation and, within the framework of the EUROfusion Consortium, by the European Union via the Euratom Research and Training Programme (Grant Agreement No 101052200 — EUROfusion). Views and opinions expressed are however those of the authors only and do not necessarily reflect those of the European Union or the European Commission. Neither the European Union nor the European Commission can be held responsible for them.

[1] ITER Organization. Iter research plan within the staged approach. *Technical Report*, ITR-18-003, 2018.

[2] H. Zohm. Edge localized modes (elms). *Plasma Physics Controlled Fusion*, 38(105), 1996.

[3] A. Loarte, G. Saibene, R. Sartori, D. Campbell, M. Becoulet, L. Horton, T. Eich, A. Herrmann, G. Matthews, N. Asakura, A. Chankin, A. Leonard, G. Porter, G. Federici, G. Janeschitz, M. Shimada, and M. Sugihara. Characteristics of type i elm energy and particle losses in existing devices and their extrapolation to iter. *Plasma Physics Controlled Fusion*, 45(1549), 2003.

[4] J.W. Coenen, G. Arnoux, B. Bazylev, G.F. Matthews, A. Autricque, I. Balboa, M. Clever, R. Dejarnac, I. Coffey, Y. Corre, S. Devaux, L. Frassinetti, E. Gauthier, J. Horacek, S. Jachmich, M. Komm, M. Knaup, K. Krieger, S. Marsen, A. Meigs, Ph. Mertens, R.A. Pitts, T. Puetterich, M. Rack, M. Stamp, G. Sergienko, P. Tamain, V. Thompson, and JET-EFDA Contributors. Elm-induced transient tungsten melting in the jet divertor. *Nuclear Fusion*, 55(023010), 2015.

[5] A. Loarte, G. Huijsmans, S. Futatani, L.R. Baylor, T.E. Evans, D. M. Orlov, O. Schmitz, M. Becoulet, P. Cahyna, Y. Gribov, A. Kavin, A. Sashala Naik, D.J. Campbell, T. Casper, E. Daly, H. Frerichs, A. Kischner, R. Laengner, S. Lisgo, R.A. Pitts, G. Saibene, and A. Wingen. Progress on the application of elm control schemes to iter scenarios from the non-active phase to dt operation. *Nuclear Fusion*, 54(033007), 2014.

[6] A. Kirk, E. Nardon, R. Akers, M. Bécoulet, G. De Temmerman, B. Dudson, B. Hnat, Y.Q. Liu, R. Martin, and P. Tamain. Resonant magnetic perturbation experiments on mast using external and internal coils for elm control. *Nuclear Fusion*, 50(034008), 2010.

[7] T. Lunt, M. Maraschek, R. M. McDermott, A. Mlynek, T. Pütterich, M. Rott, T. Vierle, E. Wolfrum, Q. Yu, I. Zammuto, , and H. Zohm (ASDEX Upgrade Team). First observation of edge localized modes mitigation with resonant and nonresonant magnetic perturbations in asdex upgrade. *Physical Review Letters*, 106(225004), 2011.

[8] R. J. Groebner, M. Groth, J. H. Harris, R. J. La Haye, C. J. Lasnier, D. G. Pretty S. Masuzaki8, N. Ohyabu8, T. L. Rhodes, H. Reimerdes, D. L. Rudakov, M. J. Schaffer, G. Wang, , and L. Zeng. Suppression of large edge-localized modes in high-confinement diii-d plasmas with a stochastic magnetic boundary. *Physical Review Letters*, 92(23500), 2004.

[9] M. Bécoulet, M. Beurskens, T. Biewer, M. Bigi, K. Crombe, E. De La Luna, P. de Vries, W. Fundamenski, S. Gerasimov, C. Giroud, M. P. Gryaznevich, N. Hawkes, S. Hotchin, D. Howell, S. Jachmich, V. Kiptily, L. Moreira, V. Parail, S. D. Pinches, E. Rachlew, , and O. Zimmermann. Active control of type-i edge-localized modes with n=1 perturbation fields in the jet tokamak. *Physical Review Letters*, 98(265004), 2007.

[10] K G McClements, R J Akers, W U Boeglin, M Cecconello, D Keeling, O M Jones, A Kirk, I Klimek, R V Perez, K Shinohara, and K Tani. The effects of resonant magnetic perturbations on fast ion confinement in the mega amp spherical tokamak. *Plasma Physics Controlled Fusion*, 57(075003), 2015.

[11] M.A. Van Zeeland, N.M. Ferraro, B.A. Grierson, W.W. Heidbrink, G.J. Kramer, C.J. Lasnier, D.C. Pace, S.L. Allen, X. Chen, T.E. Evans, M. García-Muñoz, J.M. Hanson, M.J. Lanctot, L.L. Lao, W.H. Meyer, R.A. Moyer, R. Nazikian, D.M. Orlov, C. Paz-Soldan, and A. Wingen. Fast ion transport during applied 3d magnetic perturbations on diii-d. *Nuclear Fusion*, 55(073028), 2015.

[12] M Garcia-Munoz, S Äkäslompolo, P de Marne, M G Dunne, R Dux, T E Evans, N M Ferraro, S Fietz, C Fuchs, B Geiger, A Herrmann, M Hoelzl, B Kurzan, N Lazanyi, R M McDermott, M Nocente, D C Pace, M Rodriguez-Ramos, K Shinohara, E Strumberger, W Suttrop, M A Van Zeeland, E Viezzer, M Willensdorfer, E Wolfrum, and the ASDEX Upgrade Team. Fast-ion losses induced by elms and externally applied magnetic perturbations in the asdex upgrade tokamak. *Plasma Physics Controlled Fusion*, 55(124014), 2013.

[13] J. Galdon-Quiroga, L. Sanchis-Sanchez, X. Chen, G. Birkenmeier, K. Gage, P. Cano-Megias, J. Gonzalez-Martin, W.W. Heidbrink, O. Putignano, D. Ryan, G. Suarez Lopez, B. Tal, M.A. VanZeeland, E. Viezzer, M. Willensdorfer, the ASDEX Upgrade Team, and the EUROfusion MST1 Team. Experimental investigation of beam-ion losses induced by magnetic perturbations using the light ion beam probe technique in the asdex

upgrade tokamak. *Nuclear Fusion*, 62(9), 2022.

[14] L. Velarde, J. F. Rivero-Rodríguez, J. Galdón-Quiroga, T. Williams, J. Rueda-Rueda, P. Cano-Megías, R. Chacartegui, M. García-Muñoz, S. Blackmore, and K. G. McClements. Velocity-space analysis of fast-ion losses measured in mast-u using a high-speed camera in the fild detector. *Plasma Phys. Control. Fusion*, 67(015024), 2024.

[15] G. Federici, C.H. Skinner, J.N. Brooks, J.P. Coad, C. Grisolia, A.A. Haasz, A. Hassanein, V. Philipps, C.S. Pitcher, J. Roth, W.R. Wampler, and D.G. Whyte. Plasma-material interactions in current tokamaks and their implications for next step fusion reactors. *Nuclear Fusion*, 41(1967), 2001.

[16] V. S. Mikhailova, P. Yu. Babenkoa, A. P. Shergina, and A. N. Zinovieva. Sputtering yields of beryllium and tungsten by various atoms from hydrogen to tungsten. *Plasma Physics Reports*, 50(1), 2024.

[17] Alvaro Lopez-Cazalilla, Joonas Jussila, Kai Nordlund, and Fredric Granberg. Effect of surface morphology on tungsten sputtering yields. *Computational Materials Science*, 216(111876), 2023.

[18] M. Garcia-Munoz, M. Kocan, J. Ayllon-Guerola, L. Bertalot, Y. Bonnet, N. Casal, J. Galdon, J. Garcia Lopez, T. Giacomin, J. Gonzalez-Martin, J. P. Gunn, M. C. Jimenez-Ramos, V. Kiptily, S. D. Pinches, M. Rodriguez-Ramos, R. Reichle, J. F. Rivero-Rodriguez, L. Sanchis-Sanchez, A. Snicker, G. Vayakis, E. Veshchev, Ch. Vorpahl, M. Walsh, and R. Walton. Conceptual design of the iter fast-ion loss detector. *Review of scientific instruments*, 87(11D829), 2016.

[19] A. Snicker, L. Sanchis-Sanchez, K. Särkimäki, O. Hyvärinen, J. Galdon-Quiroga, A. Rayner, R. Marques-Gomez, M.Garcia-Munoz, and J. Gonzalez-Martin. Ascot modelingfor the iter fild project. *18th Energetic Particle Technical Meeting*, 2025.

[20] A. Reynes-Vinolas and et. al. Optimizing fild pinhole and collimator. *Plasma Physics and Control Fusion*, submitted, 2025.

[21] V.G. Kiptily, C.D. Challis, R. Dumont, M. Fitzgerald, J. Garcia, L. Garzotti, Z. Ghani, J. Hobirk, P. Jacquet, A. Kappatou, D. Keeling, Ye. Kazakov, P. Mantica, M.J. Mantsinen, S.E. Sharapov, E.R. Solano, D. Van Eester, P.J. Bonofiglo, T. Craciunescu, A. Dal Molin, J. Eriksson, V. Goloborodko, M.V. Iliasova, E.M. Khilkevitch, D. King, I. Lengar, M. Nocente, S. Menmuir, M. Podesta, M. Poradzinski, D. Rigamonti, J. Rivero-Rodriguez, , Z. Stancar, , A.E. Shevelev, P. Siren, H. Sun, D.M. Taylor, M. Tardocchi, P. Beaumont, F. Belli, F.E. Cecil, R. Coelho, M. Curuia, M. Garcia-Munoz, E. Joffrin, C. Lowry, M. Lennholm, E. Lerche, C.F. Maggi, J. Mailloux, D. Marocco, M. Maslov, C. Perez Von Thun, F. Rimini, V. Zoita, and JET Contributorsa. Observation of alpha-particles in recent d–t experiments on jet. *Nuclear Fusion*, 64(086059), 2024.

[22] R. J. Akers, E. Verwichte, T. J. Martin, S. D. Pinches, and R. Lake. Gpgpu monte carlo calculation of gyro-phase resolved fast ion and n-state resolved neutral deuterium distributions. *39th EPS Conference 16th Int. Congress on Plasma Physics*, 12(pp 1–4), 2012.

[23] S. H. Ward, R. Akers, A.S. Jacobsen, P. Ollus, S.D. Pinches, E. Tholerus, R.G.L. Vann, and M.A. Van Zeeland. Verification and validation of the high-performance lorentz-orbit code for use in stellarators and tokamaks (locust). *Nuclear Fusion*, 61(086029), 2021.

[24] S. H. Ward, R. Akers, L. Li, Y.Q. Liu, A.Loarte, S.D. Pinches, A. R. Polevoi, R.G.L. Vann, and M.A. Van Zeeland. Locust-gpu predictions of fast-ion transport and power loads due to elm-control coils in iter. *Nuclear Fusion*, 62(126014), 2022.

[25] R J Akers, S Äkäslompolo, B Colling, J Hess, Y Liu, S D Pinches, K Särkimäki, M Singh, A Turner, and J Varje. High fidelity simulations of fast ion power flux driven by 3d field perturbations on iter. *IAEA Fusion Energy Conference*, 1(TH/4), 2016.

[26] S. Äkäslompolo, T. Kurki-Suonio, O. Asunta, M. Cavinato, M. Gagliardi, E. Hirvijoki, G. Saibene, S. Sipilä, A. Snicker, K. Särkimäki, and J. Varje. Iter fast ion confinement in the presence of the european test blanket module. *Nucl. Fusion*, 55(093010), 2015.

[27] L. Sanchis, M. Garcia-Munoz, E. Viezzer, A. Loarte, L. Li, Y.Q. Liu, A. Snicker, L. Chen, F. Zonca, S.D. Pinches, and D. Zarzoso. Optimizing beam-ion confinement in iter by adjusting the toroidal phase of the 3d magnetic fields applied for elm control. *Nuclear Fusion*, 61(046006), 2021.

[28] J Galdon-Quiroga, M Garcia-Munoz, M Salewski, A S Jacobsen, L Sanchis-Sanchez, M Rodriguez-Ramos, J Ayllon-Guerola, J Garcia-Lopez, J Gonzalez-Martin, and M C Jimenez-Ramos. Velocity-space sensitivity and tomography of scintillator-based fast-ion loss detectors. *Plasma Physics and Controlled Fusion*, 60(105005), 2018.

[29] G.Z. Hao, G.Q. Dong, Y.Q. Liu, Y.H. Xu, Y.F. Zhao, S. Wang, H.D. He, M. Xue, Z.J. Li, J.X. Li, C.Y. Li, L. Wang, J.Q. Xu, W. Chen, L.J. Cai, W.L. Zhong, M. Xu, and X.R. Duan. Effect of resonant magnetic perturbations including toroidal sidebands on magnetic footprints and fast ion losses in hl-2m. *Nuclear Fusion*, 63(9), 2023.

[30] Konsta Särkimäki. Efficient and rigorous evaluation of fast particle losses in non-axisymmetric tokamak plasmas. *Nuclear Fusion*, 60(036002), 2020.

[31] Jari varje and otto asunta and mario cavinato and mario gagliardi and eero hirvijoki and tuomas koskela and taina kurki-suonio and yueqiang liu and vassili parail and gabriella saibene and seppo sipilä and antti snicker and konsta särkimäki and simppa Äkäslompolo. *Nuclear Fusion*, 56(046014), 2016.

[32] L. Li, Y.Q. Liu, A. Loarte, S.D. Pinches, A. Polevoi, Y. Liang, and F.C. Zhong. Modeling 3d plasma boundary corrugation and tailoring toroidal torque profiles with resonant magnetic perturbation fields in iter. *Nuclear Fusion*, 59(096038), 2019.

[33] L. Li, Y.Q. Liu, A. Loarte, S.D. Pinches, A. Polevoi, and F.C. Zhong. Elm control optimization for various iter scenarios based on linear and quasi-linear figures of merit. *Physics of Plasmas*, 27(042510), 2020.

[34] Konsta Särkimäki, Jari Varje, Marina Bécoulet, Yueqiang Liu, and Taina Kurki-Suonio. Mechanics of elm control coil induced fast particle transport in iter. *Nuclear Fusion*, 58(076021), 2018.

[35] Y. Q. Liu, A. Bondeson, C. M. Fransson, B. Lennartson, and C. Breitholtz. Feedback stabilization of nonaxisymmetric resistive wall modes in tokamaks. i. electromagnetic model. *Physics of Plasmas*, 7(3681), 2000.

[36] L. Li, Y.Q. Liu, A. Loarte, S.D. Pinches, A. Polevoi, and F.C. Zhong. Toroidal modeling of resonant magnetic perturbations in preparation for the initial phase of iter operation. *Nuclear Fusion*, 60(016013), 2019.

[37] C. Chrystal, B.A. Grierson, G.M. Staebler, C.C. Petty, W.M. Solomon, J.S. deGrassie, K.H. Burrell, T. Tala, and A. Salmi. Predicting rotation for iter via studies of intrinsic torque and momentum transport in diii-d. *Physics of Plasmas*, 24(056113), 2017.

[38] G.M.Staebler, J.E. Kinsey, and R.E. Waltz. A theory-based transport model with comprehensive physics. *Physics of Plasmas*, 14(055909), 2007.

[39] Bo S. Schmidt, Jesús Poley-Sanjuán, José Rueda-Rueda, Joaquín Galdon-Quíroga, Marcelo Baquero-Ruiz, Henrik Järleblad, Bernard C.G. Reman, Mads Rud, Andrea Valentini, Manuel García-Muñoz, and Mirko Salewski. A new fildsim model for improved velocity-space sensitivity modelling and reconstructions. *Plasma Physics and Controlled Fusion*, 66(045004), 2024.

[40] J. Galdon-Quiroga, M. Garcia-Munoz, L. Sanchis-Sanchez, M. Mantsinen, S. Fietz, V. Igochine, M. Maraschek, M. Rodriguez-Ramos, B. Sieglin, A. Snicker, G. Tardini, D. Vezinet, M. Weiland, L.G. Eriksson, The ASDEX Upgrade Team, and The EUROfusion MST1 Team. Velocity space resolved absolute measurement of fast ion losses induced by a tearing mode in the asdex upgrade tokamak.

Nuclear Fusion, 58(036005), 2018.

[41] Jose Rueda Rueda. https://doi.org/10.5281/zenodo.12512087 - fildsim code. *Zenodo*, 10(12512087), 2024.

[42] S. Sipilä, J. Varje, T. Johnson, R. Bilato, J. Galdon Quiroga, A. Snicker, T. Kurki Suonio, L. Sanchís, D. Silvagni, J. González Martín, the ASDEX Upgrade Teama, and the EUROfusion MST Team. Ascot orbit-following simulations of ion cyclotron heating with synthetic fast ion loss diagnostic: a first application to asdex upgrade. *Nuclear Fusion*, 61(086026), 2021.

[43] J. Poley-Sanjuán, A. Jansen Van Vuuren, J. Galdón-Quiroga, S. Mazzi, M. Podestà, M.B. Dreval, B.P. Duval, A. Fasoli, A.N. Karpushov, B. Labit, U. Kumar, the EUROfusion Tokamak Exploitation Teama, and the TCV Team. First measurements of velocity-space resolved intra-elm fast-ion losses on the tcv tokamak. *Nuclear Fusion*, 65(092006), 2025.

[44] S.S. Wanga, Z.X. Zhanga, J. Huang, J.F. Chang, J. Galdon-Quiroga, L. Sanchis, W. Gao, J. Fu, Y.X. Sun, X.H. Wang, C. Shi, and the EAST Team. Beam-ion losses velocity-space distribution under neutral-beam injection on east. *Nuclear Fusion*, 65(016026), 2025.

Appendix 1: Resampling technique for enhanced statistics

This appendix section describes the technique used to enhance the statistics, its advantages and limitations, based on reference [25].

A typical LOCUST simulation, performed on a system equipped with four NVIDIA A100 GPUs operating in parallel, requires approximately 20 hours to follow the full orbit of one million markers for a duration of 100 ms, representing the typical timescale for saturation of the process from alpha particle generation in the D–T reactions to their eventual collision with PFCs. This number of markers is sufficient to estimate global transport characteristics and the overall power deposition on PFCs. However, it lacks the statistical resolution necessary to accurately quantify localised power fluxes density on geometrically complex structures or to resolve fluxes on small areas.

An accurate evaluation of the alpha and power flux density on intricate structural morphologies requires approximately 200 million markers, which demands computational resources beyond reasonable limits. Therefore, to maintain computational efficiency, an optimised resampling of markers is employed.

A preliminary run is performed by following 1 million markers for 100 ms, recording the state of each marker 0.1 to 0.2 ms (pre-lost state) before it hits any PFC. These markers are then extensively replicated in the pre-lost state and tracked again, resulting in approximately 200 million markers based on the 600,000 to 700,000 markers that hit a PFC during the preliminary run. These replicated markers are expected to hit a PFC again within a very short time window, generally around the same 0.1 to 0.2 ms that the original marker took to strike the PFC in the preliminary run. Thus, LOCUST follows the resampled markers orbits for a very short time.

The orbits of the replicated markers diverge from each other, and from the original marker, due to stochastic differences introduced by Monte Carlo collisions. To account for potential energy differences between the preliminary and resampled runs, the power is rescaled across the set of replicated markers to the respective original ones, ensuring that their combined contribution reproduces the results of the original marker, thereby maintaining consistency in the power deposition estimation.

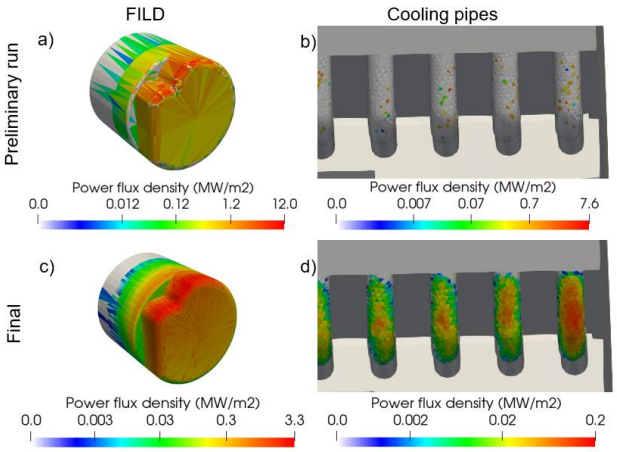

Figure 1: Comparison between the preliminary and final results, showing how the peaks of heat flux are reduced and smoothed over the surface.

The overall uncertainties from the preliminary run must still be propagated into the final results. To achieve this, bootstrap subsampling is performed based on the original markers rather than their resampled counterparts. This technique still smooths peaks of power loads and reduces the statistical uncertainty in the estimation of localised fluxes, particularly in small areas where the insufficient number of markers would otherwise introduce significant noise. Figure 1 presents a comparison illustrating the efficiency of the applied technique.

The effect on the cooling pipes beneath the dome divertor can be observed by comparing figure 1b (preliminary) and figure 1d (final). In the preliminary run (figure 1b), very small regions of concentrated power flux appear surrounded by areas with zero deposition. This is a consequence of an insufficient number of samples, leading to uncertainties in the power flux density that are comparable to the values themselves, thus making any conclusions unreliable. In contrast, figure 1d shows the power more evenly distributed over a broader area. Here, the uncertainties are within acceptable bounds, and the peak power flux can be evaluated.

On the FILD, a similar effect can be observed by comparing figure 1a (preliminary) and figure 1c (final), although it is less pronounced than in the case of the cooling pipes. The peak power loads are more accurately determined in the final result, which is critical given that the FILD is designed to operate near its tolerance limits of power flux density.

Furthermore, the resolution of the synthetic diagnostic is significantly enhanced. The first wall receives particles following the same characteristic orbits as those observed by the FILD. The improvement in the FILD strike map depends on the exchange of mark-

ers between the wall and the FILD, and as such, the resolution is not uniformly improved across all regions of the strike map. Figure 2 illustrates the differences in the strike map between the preliminary and final runs.

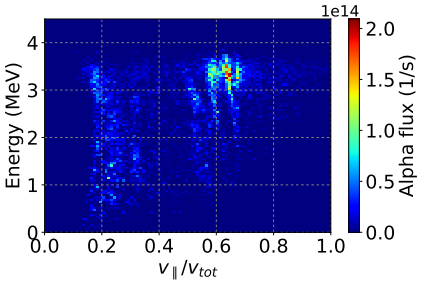

(a) Preliminary Strike map

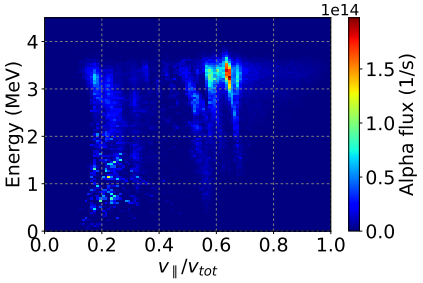

(b) Final Strike map

Figure 2: Strike maps obtained from the (a) preliminary and (b) final simulations.

The deeply trapped orbits ($v_\parallel/v < 0.5$) bounce within a short poloidal and toroidal path near the SOL, covering relatively short distances. As a result, especially the ones in the lower energy spectrum (also small Larmor radii) exhibit a lower rate of exchange between the first wall and the FILD, leading to negligible statistical improvement in their corresponding strike map regions. The 2D histogram still present characteristics related to small number of markers.

Nevertheless, these particles, which make up the majority of the lower-energy spectrum, are detected by the FILD up to 100 ms after their birth in the D-T reaction. They are responsible for a significant portion of the heat flux impacting the frontmost edge of the probe. Although replicated markers generally follow similar trajectories, they experience slight deviations due to Monte Carlo scattering in the scrape-off layer (SOL), leading them to strike different areas of the probe. The replication technique is essential for constructing a smoother distribution of power flux density, ultimately helping to reduce peak heat loads on the probe.

Improving the entire strike map requires overpopulating the markers that are born in the characteristic orbits where the strike map is still unreliable, and follow theirs orbits for the entire slowing down process, which demands more GPU resources. Moreover, it is expected that this area of the strike map overlap with deuterium bean ions, making it indistinguishable, thus out of the scope of this work.

The deeply trapped particles in the higher energy spectrum still maintain sufficient exchange between the wall and the FILD, which improves the statistical reliability in those regions of the strike map.

The broader orbits ($v_\parallel/v \geq 0.5$) travel significantly longer distances, covering both the plasma core and the SOL. This results in a substantially higher rate of exchange between the wall and the FILD. Consequently, the strike map in this region is constructed from a considerably larger number of resampled markers, replicated from multiple original ones, allowing an accurate calculation of the flux with minimal statistical uncertainty.

These two regions of the strike map compound the higher energy spectrum and their orbits intercept the FILD up to 10 ms after birth. Therefore, the replicating technique still gives substantial GPU optimization.

Moreover, the technique provides sufficient sampling in the small area around the pinhole, enabling an accurate calculation of the alpha flux in different regions of the strike map, and allowing reliable inferences about the gyro-phases that can pass through the collimator and actually strike the scintillant plate. The resulting strike maps are therefore reliable, as discussed in sections 4.2.